PAPER • OPEN ACCESS

Resonant x-ray diffraction measurements in charge ordered kagome superconductors KV_3Sb_5 and RbV_3Sb_5

View the article online for updates and enhancements.

Resonant x-ray diffraction measurements in charge ordered kagome superconductors KV$_3$Sb$_5$ and RbV$_3$Sb$_5$

Valerio Scagnoli[1,2,*] ⓘ**, Lauren J Riddiford**[1,2] ⓘ**, Shih Wen Huang**[2]**, You-Guo Shi**[3,4]**, Zhijun Tu**[5,6]**, Hechang Lei**[5,6] ⓘ**, Alessandro Bombardi**[7] ⓘ**, Gareth Nisbet**[7] **and Zurab Guguchia**[2] ⓘ

[1] Laboratory for Mesoscopic Systems, Department of Materials, ETH Zurich, 8093 Zurich, Switzerland
[2] Paul Scherrer Institute, 5232 Villigen PSI, Switzerland
[3] Beijing National Laboratory for Condensed Matter Physics and Institute of Physics, Chinese Academy of Sciences, Beijing 100190, People's Republic of China
[4] University of Chinese Academy of Sciences, Beijing 100049, People's Republic of China
[5] Department of Physics and Beijing Key Laboratory of Opto-electronic Functional Materials and Micro-nano Devices, Renmin University of China, Beijing 100872, People's Republic of China
[6] Key Laboratory of Quantum State Construction and Manipulation (Ministry of Education), Renmin University of China, Beijing 100872, People's Republic of China
[7] Diamond Light Source, Harwell Science and Innovation Campus, Didcot, Oxfordshire OX11 0DE, United Kingdom

E-mail: valerios@ethz.ch

CrossMark

Abstract

We report on (resonant) x-ray diffraction experiments on the normal state properties of kagome-lattice superconductors KV$_3$Sb$_5$ and RbV$_3$Sb$_5$. We have confirmed previous reports indicating that the charge density wave (CDW) phase is characterized by a doubling of the unit cell in all three crystallographic directions. By monitoring the temperature dependence of Bragg peaks associated with the CDW phase, we ascertained that it develops gradually over several degrees, as opposed to CsV$_3$Sb$_5$, where the CDW peak intensity saturates promptly just below the CDW transition temperature. Analysis of symmetry modes indicates that this behavior arises due to lattice distortions linked to the formation of CDWs. These distortions occur abruptly in CsV$_3$Sb$_5$, while they progress more gradually in RbV$_3$Sb$_5$ and KV$_3$Sb$_5$. In contrast, the amplitude of the mode leading to the crystallographic symmetry breaking from *P*6/*mmm* to *Fmmm* appears to develop more gradually in CsV$_3$Sb$_5$ as well. Diffraction measurements close to the V K edge and the Sb L$_1$ edge show no sensitivity to inversion- or time-symmetry breaking, which are claimed to be associated with the onset of the CDW phase. The azimuthal

---

* Author to whom any correspondence should be addressed.

© 2024 The Author(s). Published by IOP Publishing Ltd

angle dependence of the resonant diffraction intensity observed at the Sb L_1 edge is associated with the difference in the population of unoccupied states and the anisotropy of the electron density of certain Sb ions.

Keywords: charge density waves, resonant diffraction, superconductivity

1. Introduction

The recently discovered family of kagome metal compounds AV_3Sb_5 (A = K, Cs, and Rb, see [1–3]) has attracted much interest due to their rich physical states [4–15]. They exhibit a charge density wave (CDW) order which sets in at 80–110 K. In addition to CDW, superconductivity is observed below the transition temperature T_c, which varies between $\simeq 0.9$ and $\simeq 3.0$ K for different alkali metals [1–3]. T_c is further changed, reaching in some cases values as high as $\simeq 7$–8 K, either by doping [16] or application of pressure [17–19].

X-ray diffraction measurements show that the CDW is characterised by a unit cell doubling along both *a* and *b* direction, and a quadrupling along the *c* axis [20–22]. Distinct CDW phases were theoretically shown to be energetically favorable, leading to the tunability of type of CDW order by an external parameter such as temperature, pressure or doping [15, 23–27]. Experiments have also reported signatures of threefold rotational symmetry breaking inside the CDW phase [28–31]. The most important feature of the CDW state is time-reversal symmetry-breaking, which has been reported by muon-spin rotation (μSR) experiments [8, 12, 32]. Time-reversal symmetry breaking is also reflected by anisotropic intensities of the ordering vectors obtained from scanning tunneling microscopy [6, 7], field switchable chirality, a giant anomalous Hall effect [5, 33] and an anomalous Nernst signal [34]. Moreover, the chiral nature of the charge order is also supported by observed electronic magneto-chiral anisotropy [35]. Despite a tremendous amount of experimental and theoretical effort, the precise nature of symmetries broken by the CDW phase in AV_3Sb_5 remains elusive. Exploring the microscopic mechanisms responsible for the CDW formation in the AV_3Sb_5 (A = Cs, K, Rb) family of kagome metals is crucial for understanding the unique properties of the normal and the superconducting states. In this respect, an important starting point is to have a solid knowledge of the materials' crystallographic structure and its variation as a function of the alkaline atoms. To do so, we have applied advanced x-ray diffraction characterization which provides information on the crystallographic symmetry breaking occurring at the CDW formation temperature as well as the presence of an anisotropic distribution in the electron density of the V and Sb ions.

This paper is organized as follows: In section 2, we describe the sample preparation and the experimental details of the x-ray (resonant) diffraction experiment. In section 3.1, we report on the periodicity associated with the CDW phase and its temperature dependence associated with the development of a coherent long-range CDW throughout the sample. We confirm previous reports that the observed CDW periodicity

is different from the one measured in CsV_3Sb_5 and develops more gradually as a function of temperature. In section 3.2 we summarize our x-ray diffraction measurements performed in the vicinity of the V K edge and the Sb L_1 edge. In conclusion, the resonant x-ray diffraction cross section is not sensitive to the symmetry breaking associated with the occurrence of the CDW. The resonant enhancement observed at the Sb L_1 edge originates from the anisotropy of the Sb electron density.

2. Experimental details

Single crystals of RbV_3Sb_5 and KV_3Sb_5 were synthesized by Rb, K ingot (purity 99.9%), V powder (purity 99.9%), and Sb grains (purity 99.999%) using the self-flux method [3].

The resonant x-ray diffraction experiment was carried out at the I16 beamline [36] at the Diamond light Source, using a six-circle 'Kappa' diffractometer in horizontal scattering geometry equipped with a Pilatus 100 K detector from Dectris. An illustration of the experimental setup is shown in figure 5. In the experiment, a KV_3Sb_5 (RbV_3Sb_5) single-crystal sample with a surface normal direction close to [0 0 1] and an area of ~2×2 mm^2 was mounted in an ARS DE-202SK cryo cooler to stabilize the sample temperature in an interval ranging from 5 K to room temperature. The horizontally polarized x-ray beam was focused to a spot size of 20 μm $\times$ 200 μm (vertical $\times$ horizontal).

The x-ray beam energy was tuned in the vicinity of the Sb L_1 edge ($2s \rightarrow 5p$ transition) at around 4.7 keV (λ = 0.264 nm) and subsequently close to the V K edge ($1s \rightarrow 4p$ transition) at around 5.4 keV (λ = 0.229 nm).

Analysis of the polarization of the scattered x-rays was performed utilizing a LiF and a graphite crystal at the Sb and V edges, respectively.

3. Results and discussion

3.1. Superlattice peaks

Members of the AV_3Sb_5 (A = K, Rb and Cs) are known to undergo a symmetry-breaking transition that results in an increase of the unit cell size [37]. At ambient pressure, a CDW in AV_3Sb_5 sets in at $T_{CDW} \sim 78$ K, 93 K and 103 K for A = K, Cs and Rb, respectively. For CsV_3Sb_5 there have been several reports based on high energy x-ray diffraction [21, 22, 37] and resonant x-ray diffraction at the V and Sb absorption edges. [38] Few groups [21, 22, 39] have reported the occurrence of a CDW instability in CsV_3Sb_5 which is three-dimensional in nature, with a resulting $2 \times 2 \times 4$ superstructure. However, Li *et al* [38] did not observe
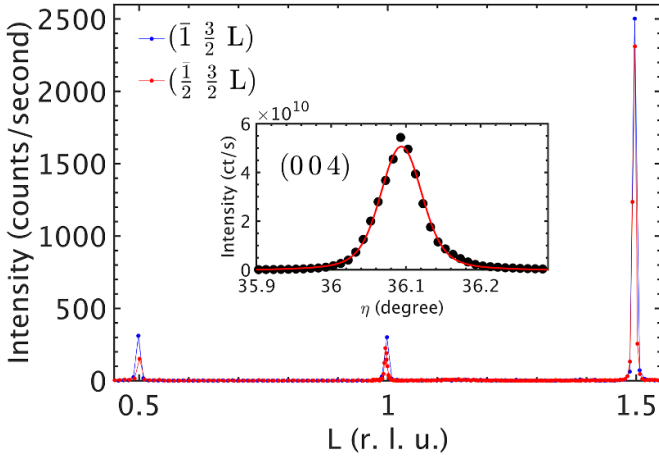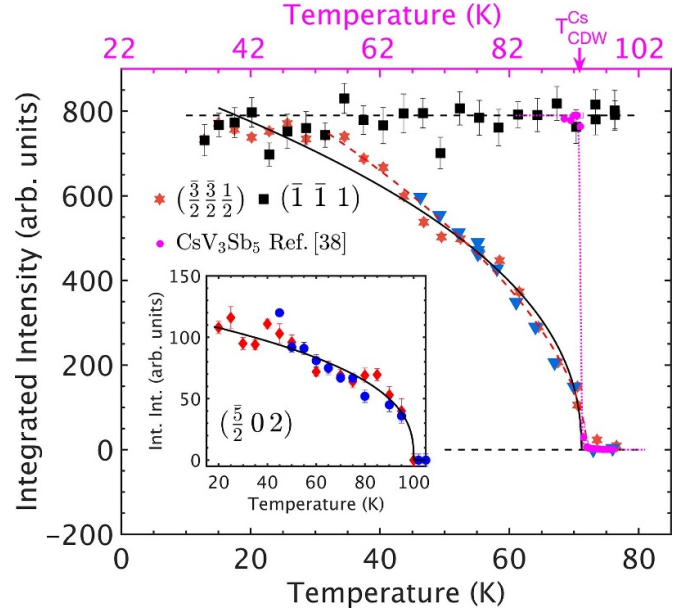
Figure 1. Reciprocal space scan along the *L* direction. Data was acquired on a KV_3Sb_5 sample at the incident photon energy of 4.698 keV at T = 12.9(2) K, in the CDW phase. The inset shows a rocking curve of the (0 0 4) reflection (black dot) gathered at T = 12.9(2) K and at 4.73 keV. A fit of the rocking curve with a pseudo-Voigt profile (red line) gives an estimated full-width at half maximum of $0.060° \pm 0.005°$.

Figure 2. Temperature dependence of superlattice peaks for the two samples: KV_3Sb_5 in the main figure and RbV_3Sb_5 in the inset. The main panel features the temperature dependence of the $(\overline{3/2}\ \overline{3/2}\ 1/2)$ and $(\overline{1}\ \overline{1}\ 1)$ peaks in KV_3Sb_5, which was collected with an incident photon energy E = 4.68 keV and after cooling the sample from room temperature to 10 K. The $(\overline{1}\ \overline{1}\ 1)$ peak (black square) has, within the errorbars, no temperature dependence, while the $(\overline{3/2}\ \overline{3/2}\ 1/2)$ intensity (red star) decreases upon approaching T_{CDW}. After heating the sample to 120 K, we monitored the intensity variation of the $(\overline{3/2}\ \overline{3/2}\ 1/2)$ peak as the sample was cooled down below T_{CDW} (blue triangle). Within the experimental uncertainties, cooling and heating runs have comparable intensity. Close magenta point, referred to the temperature axis on top of the figure, are CsV_3Sb_5 data from [38] and serve to illustrate the abrupt saturation of the CDW order parameter in CsV_3Sb_5 at $T_{CDW}^{Cs} \sim 93$ K. Inset: the temperature dependence of the RbV_3Sb_5 $(\overline{5/2}\ 0\ 2)$ peak, also showing no hysteresis in the cooling and heating run. Lines are a guide to the eye.

such modulation in their experiment. Early solutions of the CsV_3Sb_5 $2 \times 2 \times 4$ superstructure were indexed in the trigonal $P\overline{3}$ space group (No. 147) [21]. More recent experiments [37] have observed the orthorhombic distortion alluded in [21] and index the crystallographic structure with the *Cmmm* space group (No. 20).

While crystallographic experimental reports on KV_3Sb_5 and RbV_3Sb_5 are more consistent, we judged worth investigating further the CDW phase via high-resolution x-ray diffraction. Crystallographic structures are routinely determined on micron cube-size crystals. Symmetry breaking associated with small distortions of the lattice can be obscured by several factors such as the weakness of the diffraction peaks induced by the symmetry breaking and/or the presence of twins. The goal of our x-ray diffraction experiments was 1) to compare the CsV_3Sb_5 resonant diffraction results reported in [38] with the RbV_3Sb_5 and KV_3Sb_5 and 2) to confirm recent experiments [37] reporting a $2 \times 2 \times 2$ superstructure in RbV_3Sb_5 and KV_3Sb_5 and to determine the temperature evolution of the diffraction peaks associated with the symmetry lowering on a larger sample size as compared to previous x-ray reports. [20]. The first point will be discussed in detail in the next section. As for the second one, we could identify diffraction peaks associated with a $2 \times 2 \times 2$ doubling of the P6/mmm unit cell in both RbV_3Sb_5 and KV_3Sb_5. As already reported [37], we have found no evidence for the additional superstructure (x4) along the *c*-axis direction. Our results are summarized in figure 1, with a reciprocal lattice scan along the *L* direction for the $(\overline{1}\ 3/2\ L)$ and $(\overline{1/2}\ 3/2\ L)$ family of reflections. In both cases, peaks with half-integer values are visible, whilst intensity at the quarter-integer values shows no diffraction signal.

We now turn our attention to the development of CDW ordering. Several authors [22, 38, 40] have reported x-ray measurements on CsV_3Sb_5 which confirm the symmetry change occurs abruptly at a transition temperature of T~93 K,

with the intensity of the superlattice peaks reaching a maximum value at T~92 K. Our measurements of the temperature dependence of selected superlattice peaks for KV_3Sb_5 and RbV_3Sb_5 are illustrated in figure 2. KV_3Sb_5 has a CDW instability reported around 78 K and indeed we observe the appearance of diffracted intensity consistent with the doubling of the hexagonal unit cell along all the crystallographic directions. Further, we have measured the variation of the peak intensity as a function of temperature, while cooling down the sample from T > T_{CDW} to 50 K. Comparing the peak intensity on the heating and cooling run suggests that no thermal hysteresis is present and the intensity evolution as a function of temperature follows the same power law for both conditions. We have also monitored the intensity of the $(\overline{1}\ \overline{1}\ 1)$ Bragg peak associated with integer Miller indices, whose intensity is expected to be insensitive to the CDW instability. Our measurements confirm that this is indeed the case. The intensity of this Bragg peak stays constant, within error bars, for all the measured temperature ranges. Analogous measurements were also done on a RbV_3Sb_5 confirming the development of

Table 1. Symmetry-mode analysis results. By comparing the crystallographic structure in the high-temperature phase with the one reported for the $2 \times 2 \times 2$ CDW phase (trihexagonal 'TrH' deformation), we can extract the atomic displacements and describe them in terms of a basis of symmetry-adapted modes and calculate the amplitude A of the distortion modes. Amplitude values are normalized with respect to the primitive unit cell of the high-symmetry structure. The amplitude values are given in Å.

Sample	$P6/mmm$ T[K]	$Fmmm$ T[K]	$A(\Gamma_1^+)$	$A(\Gamma_5^+)$	$A(L_1^+)$	$A(L_2^+)$	$A(M_1+)$
CsV_3Sb_5	290	90	0.031	0.002	0.021	0.010	0.016
RbV_3Sb_5	290	10	0.031	0.001	0.060	0.008	0.039
KV_3Sb_5	290	10	0.030	0.024	0.045	0.008	0.025
CsV_3Sb_5	290	10	0.038	0.000	0.064	0.001	0.039

a CDW phase at 103 K. The absence of any temperature hysteresis for diffraction intensity measurements on heating and cooling conditions is also the case for RbV_3Sb_5 (see inset of figure 2). The smooth evolution and the absence of hysteresis point to a gradual increase of the lattice distortions at the origin of the CDW phase.

Overall, concerning the CDW temperature dependence, CsV_3Sb_5 differs from RbV_3Sb_5 and KV_3Sb_5. The latter two compounds have a CDW that develops over a broader temperature range, with KV_3Sb_5 plateauing around 40 K and RbV_3Sb_5 increasing continuously till the lowest temperature is measured. In contrast, in CsV_3Sb_5 it was reported that CDW peaks plateauing just below T_{CDW} [22, 37] with the abrupt appearance of phonon mode that becomes active right at T_{CDW} [41].

To gain more insight into the origin of the contrasting temperature dependence between the Cs compound and the Rb, K one, we have carried out a symmetry-mode analysis with AMPLIMODES [42, 43] for the reported crystallographic structure above and below the CDW ordering temperature. The analysis involves identifying the symmetry-breaking distortion leading to the distorted $Fmmm$ structure by attributing contributions to various symmetry-adapted modes. As input data, we used the CIF files provided in the supplementary information of [37] and tables 1 and 3 of reference [22]. In all cases, we consider the distortions from the $P6/mmm$ structure at 290 K to the low temperature $Fmmm$ $2 \times 2 \times 2$ expanded cell. Details are reported in table 1 and in the appendix A.1. Out of the five existing symmetry adapted modes, for all three compounds, the largest amplitudes are associated with Γ_5^+, L_1^+ and M_1^+ (modes are described according to the associated irreducible representations, which are labeled according to [44]). Particularly striking is the similarity of the amplitude values for CsV_3Sb_5 and RbV_3Sb_5 between 290 K and 10 K, suggesting that both compounds undergo the same amount of distortion across the examined temperature range. This is apparently in contradiction with the temperature evolution of the intensity of the CDW Bragg peaks reported in figure 2. However, this contradiction can be resolved by looking at the mode amplitude intensity of CsV_3Sb_5 between 290 K and 90 K, just below T_{CDW}, where the order parameter has already saturated. One can see that in this case the largest amplitude is associated with the Γ_5^+ mode, with a value comparable to the other two compounds at the lowest temperature. We could therefore speculate that the intensity of the CDW peaks reflects the atomic displacements associated with the Γ_5^+ mode. As it can be seen in table 3 in appendix A.2, this mode is

associated only with the Sb atom, while the L_1^+ mode involves displacements of all the atomic species present. In summary, the AMPLIMODES symmetry analysis suggests, within the limit of the available data, that lattice distortions associated with the CDW formation occur abruptly for CsV_3Sb_5 whilst they develop more gradually in RbV_3Sb_5 and KV_3Sb_5. This is in contrast with the amplitude of the mode responsible for the symmetry breaking, which seems to be developing more gradually also in CsV_3Sb_5. In this respect, the markedly different behavior observed in CsV_3Sb_5 from the other two compounds seems to stem from a subtle balance between the crystallographic structures deformation and the associated change in the band structure of the material.

3.2. Resonant x-ray diffraction

In this section, we present the results of our measurements performed in the vicinity of the V K edge and on the Sb L_1 edge on both compounds. Resonant x-ray diffraction is a combination of diffraction and spectroscopy which combines sensitivity to long-range ordering with element specificity [45–47]. It is therefore an ideal tool to probe electronic and magnetic ordering phenomena. Specifically, under appropriate conditions, resonant diffraction is sensitive to the asymmetry of the electron density of the resonant ion. For example, it was predicted that time-reversal and inversion breaking phases in the cuprate superconducting phase could be measured [48]. While resonant x-ray diffraction evidence of symmetry breaking in some Cu-based materials is controversial [49, 50], such symmetry breaking has been unambiguously observed in V_2O_3 [51] and CB_6 [52]. Such sensitivity arises from the complex nature of the polarization and angular dependence of the x-ray cross-section, when the x-ray energy is tuned in the vicinity of an absorption edge. Specifically, the inversion breaking phases reflect a departure from the description of the sample in terms of atomic orbital of different parity with non-overlapping orbitals. A hallmark of inversion symmetry breaking is the presence of sizeable absorption peaks in the pre-edge region of the absorption edge, as exemplified by the strong pre-peaks visible in the V_2O_5 and VO_2 absorption spectra [53]. In a recent paper, [11] it was proposed to use resonant x-ray diffraction to identify plausible magnetic motifs in the CDW phase, derived from the parent hexagonal structure. However, roughly at the same time Li *et al* [38] reported the absence of a resonance in the diffracting intensity in the vicinity of the V K edge for CsV_3Sb_5. On the other hand, their report supports the
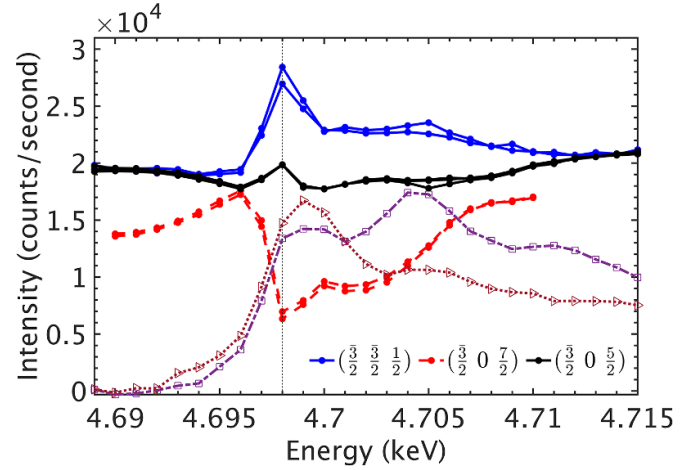
presence of a resonance in the intensity of the (1/2 0 5/2) peak near the Sb L$_1$ edge. From their observations, they deduce the presence of an Sb 5p-electron assisted CDW in CsV$_3$Sb$_5$.

The main goal of our experiment was to use resonant x-ray diffraction to identify plausible magnetic motifs associated with the development of the CDW. However, the absence of a resonance at the V K edge demonstrates that such symmetry breaking is beyond the sensitivity of the chosen technique. There could be various reasons for this lack of sensitivity; the most prominent one is that the framework developed for resonant x-ray diffraction is suitable for materials that are described best by a model based on localized electrons. Nevertheless, we can draw interesting comparisons between the behavior observed in CsV$_3$Sb$_5$ [38] with the one occurring in KV$_3$Sb$_5$ and RbV$_3$Sb$_5$.

In our experiment, we have confirmed the absence of a resonant enhancement of the intensity of the Bragg peaks associated with the CDW at the V K edge for both KV$_3$Sb$_5$ and RbV$_3$Sb$_5$ samples. However, as already reported by Li *et al* [38], a resonant enhancement for selected reflection has been observed at the Sb L$_1$ edge. In figure 3 we plot the energy dependence of the intensity of selected Bragg peaks. Only in the case of the ($\overline{3/2}$ $\overline{3/2}$ 1/2) peak there is a non-negligible enhancement of the intensity occurring 1 eV before the first maximum in the Sb K edge absorption spectra. The occurrence of the resonant enhancement of the intensity at this energy is a hallmark of the presence of a difference in the electron density of the Sb ions which contributes to the diffraction structure factor at this point in reciprocal space. Specifically, we are probing the transition from 2s states to the partially occupied 5p orbitals.

To ascertain the nature of the resonant enhancement we have performed an azimuthal angle scan of the ($\overline{1/2}$ 0 11/2) Bragg peak. This scan entails a rotation of the sample around the scattering wave vector, and the observed angular dependence provides details on the electron density distribution at the resonant atom [54]. The particular reflection was chosen as it had the most favorable condition to fulfill the experimental constraints. We collected energy scans at fixed momentum transfer for several values of the azimuthal angle ψ covering a range of ~180°. Figure 4 shows two scans performed at 95° apart. One can observe a change in the spectral shape and the development of a pronounced maximum for $\psi = -125°$, at the energy E$_A$ marked by a dashed line. To obtain a reliable azimuthal angle dependence we have normalized the intensity value recorded at E$_A$ by the values obtained at 4.68 keV. Such values measured far from the absorption edge do not depend on the angle ψ and therefore provide a means to eliminate systematic error due to the change in the diffraction geometry that occurs whilst rotating the sample around ψ.

The resulting angular dependence for KV$_3$Sb$_5$ is illustrated in the inset of figure 4 and it is characterized by a $\sin^2(\psi)$ dependence on top of a constant signal. Therefore, we can readily conclude that we observe a signal originating from the anisotropic distribution of the orbitals probed at this specific energy. To extract information on the source of the anisotropy one could use the expression provided in [55] for the resonant x-ray scattering cross-section. The experimental

Figure 3. KV$_3$Sb$_5$, selected energy scan with fixed wave vector, obtained in the vicinity of the Sb L$_1$ edge at $T = 11.2(2)$ K. For the ($\overline{3/2}$ $\overline{3/2}$ 1/2) and ($\overline{3/2}$ 0 5/2) a weak resonance is observed at $E = 4.698$ keV (marked by a black dash line), while for the ($\overline{3/2}$ 0 7/2) peak the intensity sharply decrease. Data was gathered with a Pilatus Area detector. Datasets, as they appear in the legend, are multiplied by 1, 5, and 30 respectively, for ease of comparison. Each dataset consists of two scans done at a slightly different azimuthal angle ψ value to exclude multiple scattering contributions. Open symbols represent fluorescent data collected at two different sample orientation positions (angle ϑ). Squares and triangles correspond to θ equal to 15° and 75°, respectively.
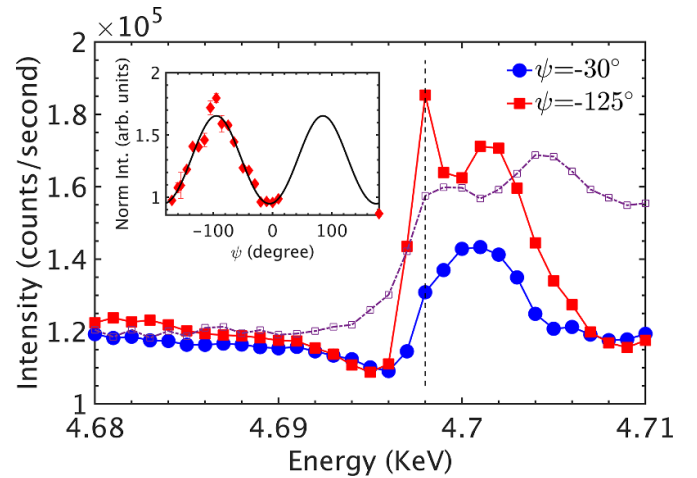
Figure 4. Energy and azimuthal dependence of the ($\overline{1/2}$ 0 11/2) Bragg peak in the vicinity of the Sb L$_1$ edge in KV$_3$Sb$_5$ at 10 K. Main panel: close symbols are measurements for fixed momentum transfer at two different azimuthal angles. The open symbol represents the normalized measured x-ray absorption of the sample. In the inset, the azimuthal angle dependence (close symbol) of the diffracted intensity for the x-ray energy of 4.698 keV is illustrated. The line is a fit of the data according to the model presented in the appendix A.2.

intensity modulation can readily be fit with two parameters, corresponding to isotropic and anisotropic scattering contributions respectively, with the former about an order of magnitude larger than the latter (see the appendix for more details).

Given the large number of independent crystallographic sites for the Sb ion in the low-temperature unit cell, it is hard to assign the observed anisotropy to a selected crystallographic site. Given the observed $\sin^2(\psi)$ azimuthal dependence we suggest that it could come from the presence of a local anisotropy direction, which is not the same for at least one of the Sb crystallographic sites. However, to be more quantitative, several azimuthal angle scans of the low-temperature crystallographic structure would be needed. This would require a dedicated experiment, given the size of the CDW unit cell, having at least 6 independent crystallographic sites for Sb. Such a feat lies outside the goal of the present manuscript.

Before concluding, we note here that there is also an increasing number of theoretical models that point to the critical role of Sb orbitals in the electronic structure and for determining the relative stability of different CDW phases. Different from Sb-ions, alkali metal ions were theoretically shown to have almost no effect on the stabilization of the CDW phase. Some of these predictions have already been confirmed by x-ray absorption experiments in CsV_3Sb_5 [56]. In the present case, the observed anisotropy of the electron density of the Sb ion in KV_3Sb_5, as well as the output of the AMPLIMODE analysis, point to a non-negligible role of Sb ions for CDW formation.

4. Conclusions

We have performed synchrotron x-ray diffraction experiments to scrutinize the periodicity of the CDW in KV_3Sb_5 and RbV_3Sb_5. We have confirmed previous reports observing a CDW associated with a $2 \times 2 \times 2$ expansion of the high-temperature P6/mmm hexagonal unit cell, which is distinct from the $2 \times 2 \times 4$ expansion reported for CsV_3Sb_5. The development of the CDW phase is distinct from the CsV_3Sb_5 one. In the latter material, the intensity of the CDW Bragg peak reaches saturation within $\sim$1 K from T_{CDW}, while for KV_3Sb_5 and RbV_3Sb_5 it develops gradually over several tens of Kelvin. Symmetry-mode analysis suggests that this behavior follows from the lattice distortions associated with the CDW formation which occur abruptly for CsV_3Sb_5 whilst they develop more gradually in RbV_3Sb_5 and KV_3Sb_5. This is in contrast with the amplitude of the mode responsible for the $P6/mmm \rightarrow Fmmm$ crystallographic symmetry breaking, which seems to be developing more gradually also in CsV_3Sb_5. Additionally, we have used resonant x-ray diffraction to ascertain the nature of the CDW in KV_3Sb_5 and RbV_3Sb_5. While resonant x-ray diffraction is potentially sensitive to inversion and time symmetry breaking, we find that this is not the case for the materials under investigation. We have found no evidence of substantial resonant enhancement of Bragg peak intensity at the V K edge. Selected reflections at the Sb L_1 edge do show some resonance, but they arise from the anisotropy of the electron density of the Sb ion and not from inversion or time symmetry breaking, as confirmed by the azimuthal angular dependence of a selected CDW peak. Such

findings establish constraints on theoretical models and they have the potential to provide guidance for future experimental investigations.

Appendix

A.1. Symmetry-adapted modes analysis with AMPLIMODES

The symmetry-adapted modes analysis presented in section 3.1 was performed using the AMPLIMODES tool provided by the Bilbao Crystallographic server within the *Solid State Theory Applications* toolbox. A detailed description of AMPLIMODES is provided in [42, 43]. Here it suffices to say that, when dealing with a change in crystallographic symmetry of a material, the structural distortions can be decomposed into contributions from different modes with symmetries given by irreducible representations of the parent space group. In this context, modes are collective correlated atomic displacements fulfilling specific symmetry properties. One could for example distinguish between primary and secondary (induced) distortions with different symmetries. The observed asymmetry between the parent and observed structures can be attributed solely to a primary distortion mode, while considering secondary distortion modes in isolation would result in a higher level of symmetry.

The tables presented in this section reproduce the results obtained with AMPLIMODES when considering the reported $P6/mmm$ (space group No. 191) as *High Symmetry Structure* and the $Fmmm$ (space group No. 69) as *Low Symmetry Structure* in the tool input. The $Fmmm$ distortion decomposes into five distortion modes of different symmetry, which are listed in table 2. Note that only the L_1^+ and L_2^+ irreducible

Table 2. Summary of the mode decomposition for the distortions associated with the symmetry breaking from *P6/mmm* to *Fmmm* in XV_3Sb_5, $X =$K, Rb, Cs. The wave vector (K-vector) involved in the distortions associated with each irreducible representation (Irrep), the direction of the order parameter as well as the isotropy subgroup, and the dimensionality of each irreducible representation are given.

K-vector	Irrep [44]	Direction	Isotropy Subgroup	Dimension
(0, 0, 0)	Γ_1^+	(a)	P6/mmm (191)	1
(0, 0, 0)	Γ_5^+	$(-1/2 \text{ a}, 0.866 \text{ a})$	Cmmm (65)	1
(1/2, 0, 1/2)	L_1^+	(a, 0, a)	Fmmm (69)	5
(1/2, 0, 1/2)	L_2^+	(a, 0, -a)	Fmmm (69)	3
(1/2, 0, 0)	M_1^+	(0, a, 0)	Pmmm (47)	4

Table 3. Summary of the basis modes. For each relevant atom in the parent unit cell, its Wyckoff position (WP) is given, as well as the irreps. Numbers in parentheses indicate the number of modes for each irrep.

| Atom	WP	Modes
Sb	4 h	$\Gamma_1^+(1)\ \Gamma_5^+(1)\ \boldsymbol{L_1^+}(2)\ \boldsymbol{L_2^+}(1)\ M_1^+(2)$
V	3f	$\boldsymbol{L_1^+}(2)\ \boldsymbol{L_2^+}(1)\ M_1^+(2)$
Cs	1b	$L_1^+(1)$

representations have the same isotropy subgroup of the low symmetry structure and can therefore be considered related to primary modes.

The set of displacements of each Wyckoff orbital of the parent structure form an invariant subspace for all symmetry operations, so that the basis modes can be chosen considering separate modes for each Wyckoff orbital in the parent structure (see table 3), The program then uses the lattice parameters and the atomic position of the high-symmetry structure to calculate a structure with the same symmetry as the low-symmetry structures. Then the lattice distortions can be compared and atomic motions can be assigned to all atoms in the unit cell.

A.2. Azimuthal angle dependence calculations

Here we describe in detail the the procedure for the fit of the azimuthal angular dependence reported in the inset of figure 4. As reported in the appendix of [55] a general expression for the structure factor F of a given Bragg reflection can be expressed in terms of atomic multipoles of rank K, with $K = 0$ (scalar/isotropic), $K = 1$ (dipole), $K = 2$ (quadrupole). $K = 2$ is the maximum rank that can be obtained for an electric dipole-electric dipole (E1-E1) transition, which is relevant in our case, as absorption and diffraction data do not suggest the need to consider other transition channels. To get an analytical expression for the structure factor, it is custom to calculate an expression for F as a function of the incident and outgoing x-ray polarization. In our experiment, we work in a horizontal scattering geometry and therefore we define the incident x-ray polarization as π. The outgoing polarization can be described in terms of its component in the scattering plane (so-called π') and in the plane perpendicular to the scattering plane (σ').

The intensity of a Bragg peak at a given momentum transfer will be given by the sum of the intensity in the two different
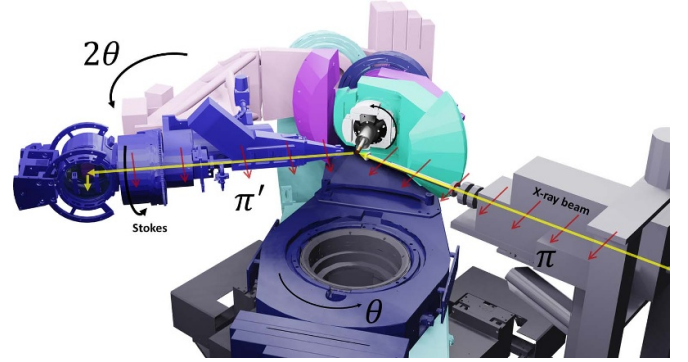
Figure 5. Experimental setup for resonant x-ray diffraction in horizontal geometry at the I16 beamline. The incident x-ray polarization is defined as π, since it is contained in the scattering plane.

outgoing polarization channels:

$$I = I_{\pi'-\pi} + I_{\sigma'-\pi} = |F_{\pi'-\pi}|^2 + |F_{\sigma'-\pi}|^2 \quad (1)$$

Measurements performed with polarization analysis prove that the intensity $I_{\sigma'-\pi}$ is negligible compare to the intensity $I_{\pi'-\pi}$. Therefore, to fit the measured azimuthal angle dependence only the $|F_{\pi'-\pi}|^2$ term needs to be taken into account.

Here we reproduce its explicit expression from [55], but without the terms which describe resonant x-ray magnetic diffraction ($A_{1,0}$ and $A_{1,1}$):

$$F_{\pi'-\pi} = -\frac{\cos(2\theta)}{\sqrt{3}} A_{0,0} - i\sin^2(\theta)\sin(2\psi) A_{2,1}^t$$
$$+ \frac{1}{\sqrt{6}}\left[\sin^2(\theta)\left(3\cos^2(\psi) - 1\right) - 1\right] A_{2,0}$$
$$+ \left[1 - \sin^2(\theta)\sin^2(\psi)\right] A_{2,2} \quad (2)$$

where $A_{K,Q}$ are linear combination of atomic multipoles of rank K. Multipoles of rank $K = 1$ ($A_{1,0}$ and $A_{1,1}$) are relevant to describe resonant magnetic scattering and are not contributing to the diffracted intensity, as the sample does not display long-range magnetic ordering.

Table 4 summarize the results of applying the expression in equation (2) to the azimuthal angle dependence obtained for the $(\overline{1/2}\ 0\ 11/2)$ Bragg peak. The minimal contribution required to describe the experimental data is given by the $A_{0,0}$ term plus either of the $A_{2,0}$ or $A_{2,2}$ contribution. Considering more than two contributions does not improve the fit.

Table 4. Parameters were obtained by fitting the azimuthal angle dependence of the $(\overline{1/2}\ 0\ 11/2)$ CDW peak with equation (2). Numbers within brackets represent standard deviations. Models 1 and 2 give the best description of the experimental data. An explicit expression for χ^2 is given in [57]. In all fits an extra parameter ψ_0 representing the deviation of the origin of the azimuthal angle is used and for all the fit $\psi_0 = 5.5° \pm 0.2°$. The origin of the azimuthal angle is chosen by setting the [1 0 0] direction as the azimuthal reference in the Diffcalc software used for reciprocal space calculation.

# fit	$A_{0,0}$	$A_{2,0}$	$A_{2,1}$	$A_{2,2}$	χ^2
1	7.31(4)	—	—	−0.47(1)	9.08
2	5.21(2)	−0.38(1)	—	—	9.08
3	5.4(2)	−0.35(4)	—	−0.03(4)	9.65
4	3.32(2)	−0.72(1)	0.32(6)	0.41(1)	9.78

Without an extended dataset of azimuthal angle dependence for several Bragg peaks is challenging to assign the source of the observed anisotropic contribution to a specific (or several) Sb atom. In general, the symmetry operations of the space group dictate the orientation of the local environment between atoms sitting at a given crystallographic (or Wyckoff) position which has higher symmetry than the most general position (x, y, z). As an example, two atoms sitting in the same Wyckoff position could be related by a rotation of 180° around a given preferential crystallographic axis. [54] In this respect, the observed two-fold azimuthal angle dependence stems from an anisotropy in the electron density that is compatible with the symmetry operation of the crystallographic space group, that characterizes the CDW phase.

ORCID iDs

Valerio Scagnoli ⓘ https://orcid.org/0000-0002-8116-8870
Lauren J Riddiford ⓘ https://orcid.org/0000-0003-0941-7040
Hechang Lei ⓘ https://orcid.org/0000-0003-0850-8514
Alessandro Bombardi ⓘ https://orcid.org/0000-0001-7383-1436
Zurab Guguchia ⓘ https://orcid.org/0000-0002-5498-328X

References

[1] Ortiz B R *et al* 2020 CsV$_3$Sb$_5$: A Z$_2$ topological kagome metal with a superconducting ground state *Phys. Rev. Lett.* **125** 247002
[2] Ortiz B R, Sarte P M, Kenney E M, Graf M J, Teicher S M L, Seshadri R and Wilson S D 2021 Superconductivity in the Z$_2$ kagome metal KV$_3$Sb$_5$ *Phys. Rev. Mater.* **5** 034801
[3] Yin Q, Tu Z, Gong C, Fu Y, Yan S and Lei H 2021 Superconductivity and normal-state properties of kagome metal RbV$_3$Sb$_5$ single crystals *Chin. Phys. Lett.* **38** 037403
[4] Kiesel M L, Platt C and Thomale R 2013 Unconventional Fermi surface instabilities in the kagome Hubbard model *Phys. Rev. Lett.* **110** 126405
[5] Yang S-Y *et al* 2020 Giant, unconventional anomalous hall effect in the metallic frustrated magnet candidate, KV$_3$Sb$_5$ *Sci. Adv.* **6** eabb6003
[6] Jiang Y-X *et al* 2021 Unconventional chiral charge order in kagome superconductor KV$_3$Sb$_5$ *Nat. Mater.* **20** 1353–7
[7] Shumiya N *et al* 2021 Intrinsic nature of chiral charge order in the kagome superconductor RbV$_3$Sb$_5$ *Phys. Rev.* B **104** 035131
[8] Mielke C *et al* 2022 Time-reversal symmetry-breaking charge order in a kagome superconductor *Nature* **602** 245–50
[9] Jiang K, Wu T, Yin J-X, Wang Z, Hasan M Z, Wilson S D, Chen X and Hu J 2022 Kagome superconductors AV3Sb5 (A = K, Rb, Cs) *Nat. Sci. Rev.* **10** nwac199
[10] Neupert T, Denner M M, Yin J-X, Thomale R and Hasan M Z 2022 Charge order and superconductivity in kagome materials *Nat. Phys.* **18** 137–43
[11] Scagnoli V, Khalyavin D D and Lovesey S W 2022 Hidden magnetic order on a kagome lattice for KV$_3$Sb$_5$ *Phys. Rev.* B **106** 064419
[12] Guguchia Z *et al* 2023 Tunable unconventional kagome superconductivity in charge ordered RbV$_3$Sb$_5$ and KV$_3$Sb$_5$ *Nat. Commun.* **14** 153
[13] Denner M, Neupert T and Guguchia Z 2022 Progress in physics: Exotic quantum phases in new kagome materials SPS Communications **68** 27 (available at: www.sps.ch/en/articles/sps-communications)
[14] Denner M M, Thomale R and Neupert T 2021 Analysis of charge order in the kagome metal *A*V$_3$Sb$_5$ (*A* = K, Rb, Cs) *Phys. Rev. Lett.* **127** 217601
[15] Christensen M H, Birol T, Andersen B M and Fernandes R M 2021 Theory of the charge density wave in *A*V$_3$Sb$_5$ kagome metals *Phys. Rev.* B **104** 214513
[16] Zhong Y *et al* 2023 Nodeless electron pairing in CsV$_3$Sb$_5$-derived kagome superconductors *Nature* **617** 488–92
[17] Chen K Y *et al* 2021 Double superconducting dome and triple enhancement of T_c in the kagome superconductor CsV$_3$Sb$_5$ under high pressure *Phys. Rev. Lett.* **126** 247001
[18] Wang N N *et al* 2021 Competition between charge-density-wave and superconductivity in the kagome metal RbV$_3$Sb$_5$ *Phys. Rev. Res.* **3** 043018
[19] Du F, Luo S, Ortiz B R, Chen Y, Duan W, Zhang D, Lu X, Wilson S D, Song Y and Yuan H 2021 Pressure-induced double superconducting domes and charge instability in the kagome metal KV$_3$Sb$_5$ *Phys. Rev.* B **103** L220504
[20] Li H *et al* 2021 Observation of unconventional charge density wave without acoustic phonon anomaly in kagome superconductors *A*V$_3$Sb$_5$ (*a* = Rb, Cs) *Phys. Rev.* X **11** 031050
[21] Ortiz B R, Teicher S M L, Kautzsch L, Sarte P M, Ratcliff N, Harter J, Ruff J P C, Seshadri R and Wilson S D 2021 Fermi surface mapping and the nature of charge-density-wave order in the kagome superconductor CsV$_3$Sb$_5$ *Phys. Rev.* X **11** 041030
[22] Stahl Q, Chen D, Ritschel T, Shekhar C, Sadrollahi E, Rahn M C, Ivashko O, Zimmermann M v, Felser C and Geck J 2022 Temperature-driven reorganization of electronic order in CsV$_3$Sb$_5$ *Phys. Rev.* B **105** 195136
[23] Ritz E T, Fernandes R M and Birol T 2023 Impact of Sb degrees of freedom on the charge density wave phase diagram of the kagome metal CsV$_3$Sb$_5$ *Phys. Rev.* B **107** 205131
[24] Hu Y, Wu X, Ortiz B R, Han X, Plumb N C, Wilson S D, Schnyder A P and Shi M 2022 Coexistence of trihexagonal and star-of-david pattern in the charge density wave of the kagome superconductor AV$_3$Sb$_5$ *Phys. Rev.* B **106** L241106
[25] Park T, Ye M and Balents L 2021 Electronic instabilities of kagome metals: saddle points and Landau theory *Phys. Rev.* B **104** 035142
[26] Lin Y-P and Nandkishore R M 2021 Complex charge density waves at van hove singularity on hexagonal lattices:

Haldane-model phase diagram and potential realization in the kagome metals AV_3Sb_5 (A=K, Rb, Cs) *Phys. Rev. B* **104** 045122

[27] Gupta R *et al* 2022 Two types of charge order with distinct interplay with superconductivity in the kagome material CsV_3Sb_5 *Commun. Phys.* **5** 232

[28] Xiang Y, Li Q, Li Y, Xie W, Yang H, Wang Z, Yao Y and Wen H-H 2021 Twofold symmetry of *c*-axis resistivity in topological kagome superconductor CsV_3Sb_5 with in-plane rotating magnetic field *Nat. Commun.* **12** 6727

[29] Zhao H, Li H, Ortiz B R, Teicher S M L, Park T, Ye M, Wang Z, Balents L, Wilson S D and Zeljkovic I 2021 Cascade of correlated electron states in the kagome superconductor CsV_3Sb_5 *Nature* **599** 216–21

[30] Nie L *et al* 2022 Charge-density-wave-driven electronic nematicity in a kagome superconductor *Nature* **604** 59–64

[31] Xu Y, Ni Z, Liu Y, Ortiz B R, Deng Q, Wilson S D, Yan B, Balents L and Wu L 2022 Three-state nematicity and magneto-optical Kerr effect in the charge density waves in kagome superconductors *Nat. Phys.* **18** 1470–5

[32] Khasanov R *et al* 2022 Time-reversal symmetry broken by charge order in CsV_3Sb_5 *Phys. Rev. Res.* **4** 023244

[33] Yu F H, Wu T, Wang Z Y, Lei B, Zhuo W Z, Ying J J and Chen X H 2021 Concurrence of anomalous Hall effect and charge density wave in a superconducting topological kagome metal *Phys. Rev. B* **104** L041103

[34] Zhou X, Liu H, Wu W, Jiang K, Shi Y, Li Z, Sui Y, Hu J and Luo J 2022 Anomalous thermal Hall effect and anomalous Nernst effect of CsV_3Sb_5 *Phys. Rev. B* **105** 205104

[35] Guo C *et al* 2022 Switchable chiral transport in charge-ordered kagome metal CsV_3Sb_5 *Nature* **611** 461–6

[36] Collins S P *et al* 2010 Diamond Beamline I16 (Materials & Magnetism) *AIP Conf. Proc.* **1234** 303–6

[37] Kautzsch L, Ortiz B R, Mallayya K, Plumb J, Pokharel G, Ruff J P C, Islam Z, Kim E-A, Seshadri R and Wilson S D 2023 Structural evolution of the kagome superconductors AV_3Sb_5 (A = K, Rb and Cs) through charge density wave order *Phys. Rev. Mater.* **7** 024806

[38] Li H *et al* 2022 Discovery of conjoined charge density waves in the kagome superconductor CsV_3Sb_5 *Nat. Commun.* **13** 6348

[39] Chen H *et al* 2021 Roton pair density wave in a strong-coupling kagome superconductor *Nature* **599** 222

[40] Wu S, Ortiz B R, Tan H, Wilson S D, Yan B, Birol T and Blumberg G 2022 Charge density wave order in the kagome metal AV_3Sb_5 (A = Cs, Rb, K) *Phys. Rev. B* **105** 155106

[41] Ratcliff N, Hallett L, Ortiz B R, Wilson S D and Harter J W 2021 Coherent phonon spectroscopy and interlayer modulation of charge density wave order in the kagome metal csv_3sb_5 *Phys. Rev. Mater.* **5** L111801

[42] Orobengoa D, Capillas C, Aroyo M I and Perez-Mato J M 2009 AMPLIMODES: symmetry-mode analysis on the Bilbao Crystallographic Server *J. Appl. Crystallogr.* **42** 820–33

[43] Perez-Mato J M, Orobengoa D and Aroyo M I 2010 Mode crystallography of distorted structures *Acta Crystallogr.* A **66** 558–90

[44] Cracknell A P, Davies B L, Miller S C and Love W F 1979 *Kronecker Product Tables. Vol. 1. General Introduction and Tables of Irreducible Representations of Space Groups* (IFI/Plenum)

[45] Lovesey S W and Collins S P 1996 *X-Ray Scattering and Absorption by Magnetic Materials* (Clarendon)

[46] Murakami Y *et al* 1998 Resonant x-ray scattering from orbital ordering in $LaMnO_3$ *Phys. Rev. Lett.* **81** 582

[47] Fink J, Schierle E, Weschke E and Geck J 2013 Resonant elastic soft x-ray scattering *Rep. Prog. Phys.* **76** 056502

[48] Di Matteo S and Varma C M 2003 Symmetry considerations for detection of time-reversal breaking phases in cuprates by x-ray diffraction and absorption *Phys. Rev.* B **67** 134502

[49] Scagnoli V, Staub U, Bodenthin Y, de Souza R A, García-Fernández M, Garganourakis M, Boothroyd A T, Prabhakaran D and Lovesey S W 2011 Observation of orbital currents in CuO *Science* **332** 696–8

[50] Lovesey S W, Scagnoli V, Dobrynin A N, Joly Y and Collins S P 2014 Effects of dispersion and absorption in resonant Bragg diffraction of x-rays *J. Phys.: Condens. Matter* **26** 125504

[51] Fernández-Rodríguez J, Scagnoli V, Mazzoli C, Fabrizi F, Lovesey S W, Blanco J A, Sivia D S, Knight K S, de Bergevin F and Paolasini L 2010 Experimental evidence of anapolar moments in the antiferromagnetic insulating phase of V_2O_3 obtained from x-ray resonant Bragg diffraction *Phys. Rev. B* **81** 085107

[52] Matsumura T, Yonemura T, Kunimori K, Sera M and Iga F 2009 Magnetic field induced $4f$ octupole in ceb_6 probed by resonant x-ray diffraction *Phys. Rev. Lett.* **103** 017203

[53] Nomura K 2019 Solution X-ray absorption spectroscopy (XAS) for analysis of catalytically active species in reactions with ethylene by homogeneous (Imido)vanadium(V) complexes-al cocatalyst systems *Catalysts* **9** 1016

[54] Lovesey S, Balcar E, Knight K and Rodríguez J F 2005 Electronic properties of crystalline materials observed in x-ray diffraction *Phys. Rep.* **411** 233–89

[55] Scagnoli V and Lovesey S W 2009 Analysis of azimuthal-angle scans in resonant x-ray Bragg diffraction and parity even and odd atomic multipoles in the multiferroic modification of the terbium manganate $TbMnO_3$ *Phys. Rev. B* **79** 035111

[56] Han S *et al* 2023 Orbital-hybridization-driven charge density wave transition in CsV_3Sb_5 kagome superconductor *Adv. Mater.* **35** 2209010

[57] The agreement between the observed and calculated intensity is estimated via $\chi^2 = \sum_i \left[\{y_i - f(x_i)\} / \sigma_i \right]^2 / (n_p - n_{par})$, where y_i are the experimental data, $f(x_i)$ are the calculated values, σ_i represent the error bars, n_p the number of point measured and n_{par} the number of free parameter in the fit.